Document Version
Final published version

Licence
CC BY

Citation (APA)
Georgopoulos, P., Sodja, J., & De Breuker, R. (2026). Camber-twist morphing flap concept with two chordwise degrees-of-freedom. *Journal of Intelligent Material Systems and Structures*. https://doi.org/10.1177/1045389X261426631

SI-ICAST2025

Journal of Intelligent Material Systems and Structures

Journal of Intelligent Material Systems and Structures
1–15

DOI: 10.1177/1045389X261426631
journals.sagepub.com/home/jim
Sage

Camber-twist morphing flap concept with two chordwise degrees-of-freedom

Panagiotis Georgopoulos[1], **Jurij Sodja**[1] **and Roeland De Breuker**[1]

Abstract

This article presents a novel camber-twist morphing flap concept with two chordwise degrees-of-freedom. The flap is capable of reflexed airfoil morphing, thereby decoupling lift from the aerodynamic moment with respect to the aerodynamic centre. The theoretical potential of such a flap is calculated via XFOIL for arbitrary trailing edge shapes, revealing ellipse-like clusters in the lift-moment plane for each value of angle of attack. A conceptual design is proposed, capable of the above functionality. Key features include two spanwise slits along the pressure side skin joined by a flexible structure, with a spar placed between them and two pairs of linear electric motors. The design is validated numerically using a nonlinear aeroelastic analysis toolchain, iterating between the finite element model of the flap and XFOIL. The attainable range of lift-moment combinations is calculated, forming an ellipse-like cluster determined by actuator stroke and force limits. The morphing flap achieves a lift-to-drag ratio of over 104.3 over a range of angles of attack. A high degree of twist morphing range is demonstrated by fixing one pair of actuators and varying the strokes on the other. The range of attainable shapes on the free end is coupled to the fixed end strokes.

Keywords

morphing flap, camber, twist, reflexed airfoil, conceptual design, aeroelastic analysis

Introduction

In recent years, two major factors have driven research and development in aviation: the dangers associated with climate change and the anticipated growth in air traffic (Jensen et al., 2023). Both factors indicate an urgent need for more efficient aircraft. This can be achieved by a combination of higher propulsive efficiency, reduced drag force and reduced aircraft weight, as suggested by the Breguet range equation (Anderson, 2016).

Morphing wings have the potential to yield increased flight efficiency in the latter two ways. One of the many definitions offered in literature describe them as "*wings that change shape in flight in a controlled manner to improve aircraft performance*" (Vasista et al., 2012). The same authors highlight the changing mission environment during flight and the need for aircraft to adapt accordingly by means of smooth and continuous shape change. Based on the above, a variety of concepts have been developed, as outlined by numerous review papers (Barbarino et al., 2011; Harvey et al., 2022; Vasista et al., 2012; Weisshaar, 2013). These studies identify several morphing modes, each with their respective strengths and weaknesses. Of particular interest are "camber morphing" and "twist morphing." Camber morphing improves the lift-to-drag ratio C_l/C_d, compared to a conventional hinged flap, whereas twist morphing controls the spanwise lift distribution (Harvey et al., 2022). Combined, the two morphing modes can reduce both profile and induced drag. Also, spanwise lift control can be used to minimise manoeuvre and gust loads, thereby leading to a lighter wing structure (Wang et al., 2021).

Such morphing wings first made their appearance on the Wright Flyer, whose flexible wings employed twist morphing for roll control (Weisshaar, 2013). After several decades, camber morphing concepts were revisited in the 1980s by the National Aeronautics and Space Administration (NASA) and the Defence

---

[1] Aerospace Structures and Materials, Aerospace Structures and Materials, Faculty of Aerospace Engineering, Delft University of Technology, The Netherlands

Corresponding author:
Panagiotis Georgopoulos, Aerospace Structures and Materials, Faculty of Aerospace Engineering, Delft University of Technology, Kluyverweg 1, Delft 2629 HS, The Netherlands.
Email: p.georgopoulos@tudelft.nl

Advanced Research Projects Agency (DARPA) in the quest for manoeuvre and gust load alleviation, as well as delayed aileron reversal (Pendleton et al., 2000; Perry et al., 1995; Powers et al., 1992). In the following decades more projects followed in the United States (Jenett et al., 2017; McGowan et al., 2002; Sanders et al., 2004) as well as Europe (De Gaspari et al., 2014; Schweiger et al., 2002; Wölcken and Papadopoulos, 2016) among others. Some notable recent studies include the following. Starting with small-scale studies, the bio-inspired Fish Bone Active Camber (FishBAC) concept demonstrated increased aerodynamic efficiency relative to a hinged flap wing. Lift-to-drag ratio improvements of over 20% were measured via wind tunnel testing over a range of pre-stall angles of attack (Woods et al., 2014). In a different study, Molinari et al. (2016) integrated morphing ailerons in the wings of a $1.75m$-span unmanned aerial vehicle, demonstrating the ability to achieve the target lift and rolling moments during flight. Combined camber and twist morphing was investigated in the Variable Camber Continuous Trailing Edge Flap (VCCTEF) programme, where multiple camber morphing flaps were seamlessly connected with the aim of spanwise aerodynamic load control (Nguyen et al., 2015). The short list of full-scale studies includes the Clean Sky programme, where a full-scale morphing flap corresponding to a 100-seat regional turboprop aircraft was built and tested in static conditions (Pecora, 2021). Finally, the Adaptive Compliant Trailing Edge (ACTE) programme stands out, where a morphing flap was installed in the wings of a Gulfstream III business jet, validating the technology via full-scale flight testing (Kota et al., 2016).

Among the many concepts found in literature, the TRanslation Induced Camber (TRIC) concept by the Delft University of Technology stands out for its simplicity. The key feature behind the TRIC is a spanwise slit running along the pressure side skin. The disconnected skin is allowed to translate with respect to the wingbox, morphing the trailing edge (TE) in the process. The above mechanism allows a lightweight design built of conventional skin materials at a minimal drag penalty. This principle has been leveraged by more concepts in literature (Cavalieri et al., 2024; Keidel et al., 2021; Moulton and Hunsaker, 2021). After its original inception as a twist morphing flap (Vos et al., 2010), the camber morphing functionality was added in the EU FP7 CHANGE project (Werter et al., 2016) and further refined in its latest implementation in the Smart-X project (De Breuker et al., 2022). The Smart-X iteration features a pair of electric motors, one on each spanwise end, joined to the wingbox skin and connected via push rod to the end of the pressure side skin. Symmetric actuation induces camber morphing whereas asymmetric actuation induces twist morphing (Mkhoyan et al., 2022). By placing six morphing flaps along the span of a prototype wing, wind tunnel testing demonstrated the morphing wing's ability to minimise induced drag (Mkhoyan et al., 2023) and alleviate manoeuvre and gust loads (Wang et al., 2021).

A less explored design approach features multiple chordwise degrees-of-freedom (DoF), with two notable studies performed by Pankonien et al. (2015) and Wu et al. (2017). First, the additional DoF helps induce larger morphing deformations. Second, a synergistic combination of actuators can be used to achieve the conflicting goals of the actuation subsystem. Most importantly, the additional DoF offers greater control over the morphing flap shape. Wind tunnel tests by Wu et al. demonstrated the ability to control the coefficient of aerodynamic moment with respect to the aerodynamic centre C_{mac} independently of the lift coefficient C_l (Wu et al., 2017). This is achieved by morphing into reflexed shapes, whose superior aerodynamic performance has been the topic of ongoing research (Harvey et al., 2022). These airfoils are characterised by a change in the sign of the camber line curvature. The resulting change in pressure distribution allows control of C_{mac}.

Reflexed airfoil morphing offers two potential advantages towards aircraft-level drag reduction. The first lies in the ability to morph into a wider selection of airfoil shapes, further minimising the drag coefficient C_d on the airfoil-level. The second advantage targets induced drag $C_{D,i}$ during flight. Conventionally, a negative lift L_t is exerted by the tail to achieve equilibrium in pitch. In the presence of a negative L_t, the wings must exert additional lift to maintain altitude. Since $C_{D,i}$ is proportional to the square of the wing lift coefficient $C_{L,w}$, the negative L_t causes an increase in $C_{D,i}$. The ability of reflexed airfoils to generate a more positive (nose-up) C_{mac} for given C_l reduces the dependence on negative L_t to achieve pitch equilibrium. Ultimately, the above mechanism reduces $C_{L,w}$ and by extension trim drag, thereby motivating the adoption of morphing wings capable of reflexed airfoil morphing.

This article presents a novel camber-twist morphing flap concept. The design uses the latest implementation of the TRIC concept as inspiration and extends its functionality to morph into reflexed shapes. The rest of this article is structured as follows. In Section 2, the potential of the novel morphing functionality is explored, in terms of attainable aerodynamic polars. A conceptual design is presented in Section 3 with emphasis on key components. Accordingly, a finite element model (FEM) is constructed in MSC Nastran (MSC Software Corporation, 2019) and presented in Section 4. The FEM is combined with XFOIL (Drela, 1989) to form an iterative nonlinear static aeroelastic analysis toolchain, with the purpose of assessing the proposed concept. The range of the camber and twist morphing functionalities is assessed in Section 5. Finally, Section 6 highlights the main conclusions from this study.

Reflexed airfoil morphing aerodynamics

High shape versatility is a key objective for morphing wing designs. In this concept, this translates to a wide range of attainable C_l-C_{mac} combinations. Ultimately, the morphing flap aims to achieve these polars at the lowest C_d possible. Prior to developing the conceptual design, the theoretical potential of a morphing flap can be demonstrated by calculating the range of attainable polars. This is achieved by globally sampling the possible TE shapes. Upon concept development, the morphing flap shapes form a subset of the sampled shapes and by definition the attainable polars are enclosed by this theoretical limit.

An airfoil parametrisation method is employed to sample the shapes. Focussing on TE morphing, a method is required which keeps the leading edge (LE) geometry unchanged. Hence, the chosen approach is modelled after the Bezier-PARSEC method (Derksen and Rogalsky, 2010). Specifically, the method splits the airfoil into LE and TE, ultimately requiring two camber lines and two half-thickness lines. Each of the four lines is modelled as a 4^{th}-order polynomial. The authors of that study proposed a method to obtain the polynomial coefficients based on physical quantities such as camber line angle and half-thickness at the trailing edge tip.

In the present study, the presence of numerous boundary conditions reduces the total number of variables from 20 to 4. Primarily, the LE geometry is fixed, eliminating the 10 variables related to the 2 LE lines. By extension, 0^{th}-order and 1^{st}-order continuity is enforced on both camber and half-thickness lines, between leading and trailing edge, eliminating two variables from each polynomial. In addition, some boundary conditions pertinent to the TRIC concept must be accounted for. First, the concept features glass fibre skins which are bonded spanwise with epoxy at the TE tip. This fixes the half-thickness line and its slope to the values of the unmorphed shape, removing two more variables. Second, the suction side skin maintains its arclength. Given the above parametrisation, the NACA0012 airfoil is chosen as the baseline shape and the morphing TE onset is set at the 60%-chord position.

Some examples of airfoils are generated using the above parametrisation and shown in Figure 1, relative to the NACA0012. The constraints pertinent to the 60%-chord position and the TE tip can be seen in the half-thickness line and camber line. The TE tip is displaced forward as a result of enforcing constant suction side skin arclength. The three major morphing shape categories are displayed. First, a "conformal" shape, characterised by the monotonic curvature of the camber line. Conversely, reflexed shapes are characterised by a change in the sign of the curvature, as seen in Figure 1. These shapes are further split into "positively reflexed" and "negatively reflexed."

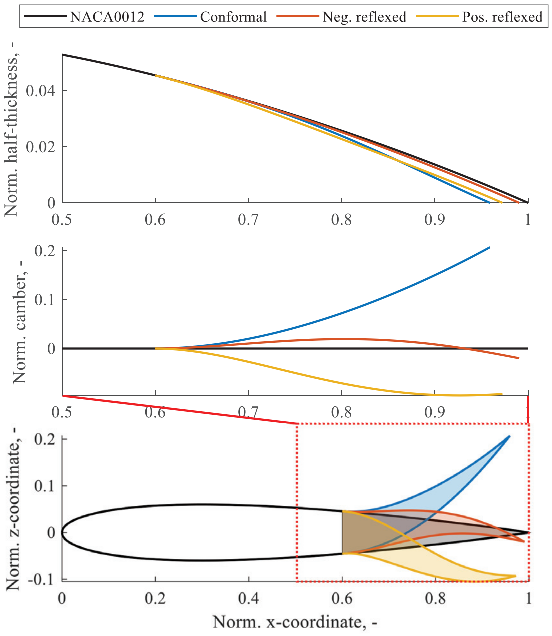

Figure 1. Airfoil geometry parametrisation method. The half-thickness and camber lines are shown for the NACA0012 and three morphed airfoils, with emphasis on the aft half of the airfoil.

With the above parametrisation, airfoil shapes are generated and supplied to XFOIL for two-dimensional (2D) steady viscous aerodynamic analysis. It is noted that the concept is developed in the context of a wind tunnel prototype to be tested in the $2.25m$-by-$3m$ Low Speed Tunnel (LST) of the German-Dutch Wind Tunnels (DNW; German-Dutch Wind Tunels, n.d.). This introduces a maximum free stream velocity $V = 80m/s$ and chord length $c = 0.8m$. Assuming ambient temperature at sea level $T = 5^{\circ}C$, the corresponding air density $\rho = 1.27kg/m^3$ and dynamic viscosity $\mu = 1.74 \times 10^{-5}kg/ms$ lead to Reynolds number $Re = 4.67 \times 10^6$ and free stream dynamic pressure $q = 4.06kPa$. The above conditions drive the results shown in this article. For each shape, the analysis is performed over a range of angle of attack values $\alpha = \{-5, -4, \ldots, 12\}^{\circ}$ and the polars are calculated. It is noted that the accuracy of XFOIL results is compromised in the presence of flow separation (Adeel-Ur-Rehman et al., 2024). This is observed at extreme values of α and highly morphed TE shapes. Nevertheless, XFOIL accuracy is sufficient to reveal the trends discussed in this section.

For given α, the polars can be plotted in three-dimensional (3D) space, with C_d on the z-axis for

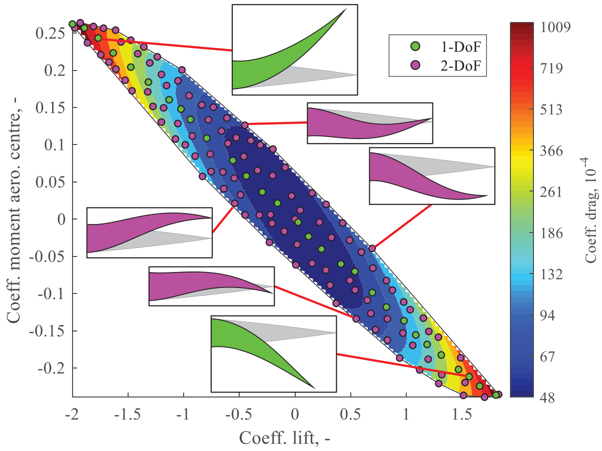

Figure 2. Theoretical limit of C_l-C_{mac} combinations for $\alpha = 0°$. Contours represent the variation of C_d within the cluster. Highlighted trailing edge shapes indicate the airfoil geometry associated with respective regions of the cluster. Samples lying along a curve demonstrate the difference between 1-DoF and 2-DoF camber morphing.

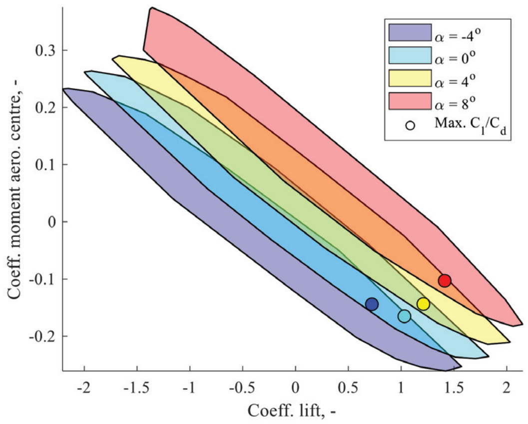

Figure 3. Evolution of clusters of attainable polars over a range of α. For each α value, the airfoil of maximum C_l/C_d is presented in terms of the corresponding C_l-C_{mac} combination.

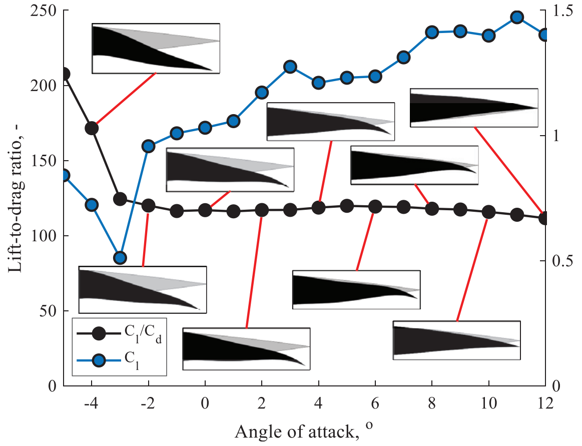

Figure 4. Maximum C_l/C_d values over a range of α, along with the corresponding C_l values. Highlighted trailing edge shapes indicate the optimal airfoil geometry.

convenience. Given the possibility to obtain airfoils of equal C_l and C_{mac} but different C_d, the focus lies on the subset of airfoils with minimum C_d for given C_l and C_{mac}. This subset forms a 2D-surface embedded in 3D-space, as shown in Figure 2 for $\alpha = 0°$. Starting from a symmetric baseline shape, the maximum attainable C_l exceeds 1.8. The C_d contours indicate the steep increase in C_d corresponding to higher values of C_l. The tick marks on the colorbar indicate the contour boundaries. The range of polars projected in the C_l-C_{mac} space is enclosed by a convex curve. As seen from the highlighted shapes, the range is enclosed by reflexed shapes; positively reflexed on the upper C_{mac} end and negatively reflexed on the lower C_{mac} end. Conversely, conformal airfoil shapes are observed in-between. An important distinction lies between 1-DoF and 2-DoF shapes. The former subset lies along a line, such that C_l and C_{mac} are coupled, resembling conventional camber morphing flap functionality, with a single chordwise actuator. The samples highlighted in Figure 2 were chosen arbitrarily to visualise this functionality.

The evolution of the clusters over a range of α is presented in Figure 3. For each value of α, the polars exhibit the above behaviour, forming convex clusters. Between $\alpha = -4°$ and $\alpha = 4°$ the clusters maintain their shape, showcasing primarily an increase in C_l and secondarily an increase in C_{mac}. The above trends are less pronounced in the case of $\alpha = 8°$. The cluster shape deviates from the shape observed in lower values of α, particularly at the extreme C_l ends. Cluster boundaries are defined by highly morphed TE shapes, therefore these airfoils experience flow separation, causing deviations in the cluster shape. Given the discussed limitations in XFOIL's predictive ability, no results are shown for higher values of α. Furthermore, the shapes of maximum C_l/C_d are found for each subset of polars. Their position on the clusters is indicated with markers. As α increases, the markers move within the cluster, indicating the need for different geometry. The overlapping clusters suggest that a given C_l-C_{mac} combination is attainable over a range of α. However, a different airfoil shape would be required, also causing a change in C_d. Finally, it is worth noting that the range of attainable C_{mac} maintains a value over 0.11 for $C_l = 0.5$, across the range of α. Hence, regardless of α, a high degree of control over the value of C_{mac} is maintained. Given the value of C_l, this observation indicates the concept's potential towards induced drag minimisation during cruise.

The variation of maximum C_l/C_d over a range of α is shown in Figure 4. A C_l/C_d value of over 111.6 is

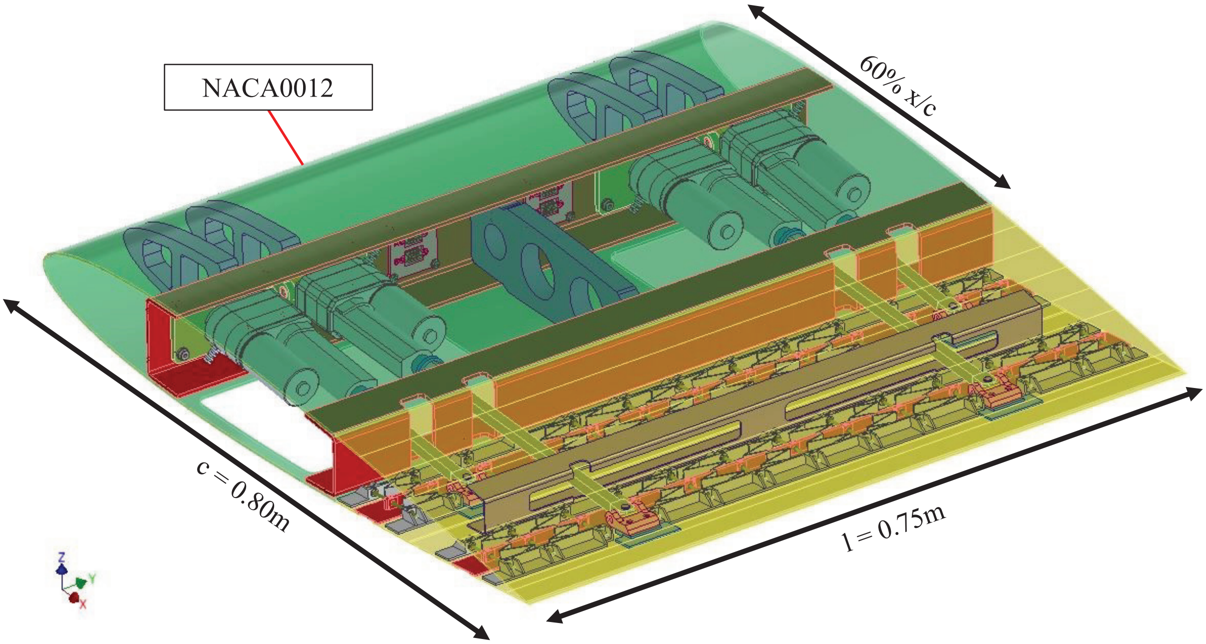

Figure 5. Morphing flap design. Annotations indicate key dimensions and the chordwise onset of the morphing trailing edge.

maintained for all α with a sharp increase in C_l/C_d below $\alpha = -3°$, reaching a maximum of 207.6. The corresponding values of C_l are also plotted. Starting from $\alpha = -2°$, C_l increases as α increases, suggesting a corresponding increase in C_d to maintain an approximately constant value of C_l/C_d. This is not the case below $\alpha = -3°$, where an increase in C_l is observed, leading to higher values of C_l/C_d. The shapes of maximum C_l/C_d reveal some trends in optimal airfoil geometry. Primarily a reduction in camber is observed, as lift is generated more and more through the increasing α. In addition, the airfoils exhibit a downwards deflection at the TE tip. Indeed, negatively reflexed shapes are observed from $\alpha = 4°$ onwards. For the lower range of α, the camber line curvature appears to change sign twice. The above indicates the importance of increased control over the TE geometry. It is noted that the calculated C_l/C_d distribution and optimal shapes are coupled to the baseline airfoil shape and the chordwise position of trailing edge onset. Also, unlike the calculation of clusters, these results focus solely on high-performance airfoils. The associated high values of C_l/C_d suggest limited flow separation, thereby justifying the use of XFOIL up to $\alpha = 12°$.

Morphing flap conceptual design

The functionality discussed in the previous section serves as a target for the morphing flap. In this section, the conceptual design is presented, with emphasis on individual components. As mentioned in Section 2, the design is developed in the context of a wind tunnel testing campaign, introducing some boundary conditions. The envisioned prototype wing has span length $L = 2.25m$, chord length $c = 0.8m$ and features three identical morphing flaps of span length $l = 0.75m$ each, with no sweep or taper. The tunnel's maximum wind speed is $V = 80m/s$; the resulting dynamic pressure drives the structural design and actuator selection. The morphing flap design is shown in Figure 5. The depicted right-handed coordinate system definition is maintained throughout the paper. Specifically, the x-axis is defined positive along the chord-line in the streamwise direction and the y-axis is defined positive in the port-to-starboard direction. The origin is defined at the port-side LE tip. An additional section view focussed on the trailing edge is shown in Figure 6, indicating some key components with annotations. The following discussion focuses on the TE design. The LE is shown for completeness but its design serves an auxiliary role, beyond the scope of this paper. Overall, the design is not the product of optimisation. Instead, it is a viable design which demonstrates the desired functionality.

As stated in Section 1 of the paper, the latest iteration of the TRIC concept serves as inspiration for this design. Accordingly, the skin is made of a glass fibre-reinforced epoxy laminate, using 0°/90° twill fabric. The plies are oriented parallel to the y-axis, aiming to provide the desired bending stiffness to mitigate aeroelastic deflections whilst allowing a large range of twist-morphing shapes. Chordwise skin stiffness is tailored via ply-dropping, to reduce the required actuation forces. A key feature to achieve reflexed shapes is the

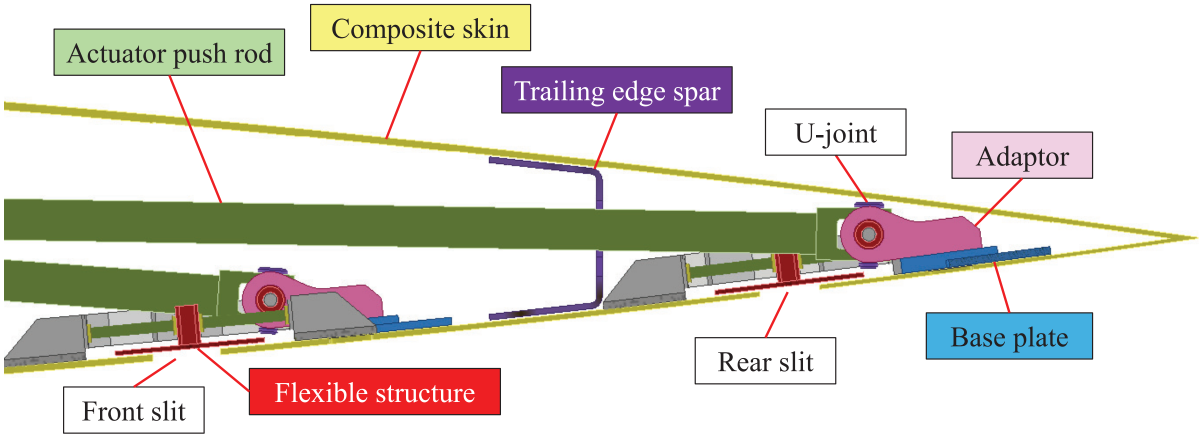

Figure 6. Trailing edge section view on a plane parallel to the x-z plane. Annotations indicate characteristic design features.

rear spanwise slit on the pressure side skin, in addition to the front slit running parallel to the rear spar. Chordwise translation in opposite directions causes the curvature to change sign, yielding reflexed shapes.

With regards to connecting the discontinuous skin, past implementations featured a stiff guide slot, whereby the aft skin was constrained vertically and was allowed to slide in-plane, remaining in contact with the front skin. The above solution is not applicable in the rear slit. The conventional stiff guide slot would greatly limit the range of the twist morphing functionality. Conversely, a flexible guide slot would risk jamming during twist morphing, as a result of slot profile warping. Instead, a flexible skin structure is used, inspired by a past span morphing concept (Bubert et al., 2010), as shown in Figure 7. The structure is characterised by two 3D-printed Nylon-12 components: a “frame” bonded to the skin on either ends of the slit and a “slider” covering the gap left by the slit with its flange and connected to the frame via flexible leaf springs joined to its web, allowing chordwise translation. Bending stiffness is imparted by $3mm$ diameter steel rods, supported by brass bushings to reduce friction and mitigate the risk of jamming. The rods are placed $60mm$ apart, overall approximating the glass fibre skin’s stiffness, maintaining curvature continuity. The pattern depicted in Figure 7 is repeated along the span. The leaf springs are omitted and local gaps are introduced locally in the slider web to prevent interference with push rods.

The actuation requirements reflect the desired functionality. The above paragraphs highlighted the importance of two slits for 2-DoF morphing. Hence, a pair of actuators is needed along the chord, with one actuator joined to the aft end of each slit. Two such pairs are needed, placed symmetrically on each spanwise end of the flap, to impart the twist morphing functionality. Ultimately, symmetric actuation between the two pairs leads to camber morphing. Conversely, asymmetric actuation induces twist morphing. The present choice of actuators was driven by stroke, blocked force, simplicity, compactness and cost, opting for commercially available, linear electric motors. All viable options were too large to fit in the TE, hence the motors are located in the wingbox. The front end of the actuators is attached to the front spar web. Actuation force is then transmitted to the pressure side skin via push rods. This amounts to a parallel connection, which is beneficial for conformal morphing shapes, as the front and rear motor apply forces in the same direction. The contrary is true for reflexed morphing shapes, which are associated with opposing chordwise translation at the slits. To achieve these shapes, the front and rear motor must oppose each other, thereby requiring high actuation forces. Using the developed analysis tool and insight from commercially available options, the DSZY1-24-40-050-POT-IP65 is selected as it meets the above criteria whilst providing $1kN$ blocked force and $50mm$ stroke (MSW Motion Control GmbH, n.d.), which are considered sufficient. This choice drives the actuators’ spanwise positioning. In the interest of achieving a high

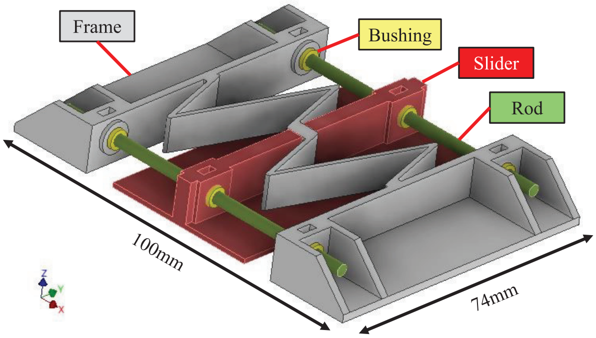

Figure 7. Focused view of flexible skin structure segment. Annotations indicate the dimensions and characteristic design features. The depicted segment is repeated along the y-axis, covering the spanwise length of the pressure side skin.

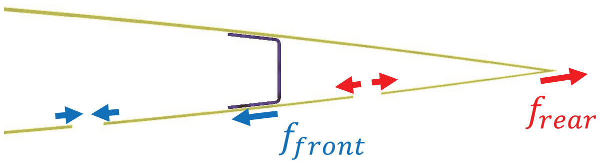

Figure 8. Schematic representation of the principle behind reflexed airfoil morphing. Chordwise translation at the slits induces forces in opposite directions. The trailing edge spar transmits moments between the two skins, resulting in the corresponding skin curvature.

degree of twist morphing, the actuators are placed towards the spanwise ends of the flap. However, adaptor plates are needed to connect to the front spar web. The plate width extends beyond the width of the actuator housing, to allow tool access to bolts in the corners for assembly. As a result, the two front actuators are displaced towards the interior, to the 13.33%-span and the 86.67%-span position. Equivalently, the two rear actuators are placed further inwards at the 22.67%-span and 77.33%-span position.

The actuators are connected to the structure on both ends via universal-joints, which allow rotations along the y-axis, associated with camber morphing, as well as the z-axis, associated with twist morphing. In the front end a universal-joint connects the motor housing to an adaptor plate, which is fixed on the front spar web. Similarly, a universal-joint connects the push rod end to an adaptor plate, which is fixed to a base plate. The base plate is bonded to the skin, thereby transmitting actuator force to the pressure side skin. Ultimately, this corresponds to an open-loop linkage, such that the morphing flap will be subject to aeroelastic deformations. These deflections are limited to an acceptable magnitude by tailoring the skin stiffness accordingly.

Finally, a TE spar is included between the two slits. This component is crucial to achieve reflexed airfoil morphing. The underlying principle is demonstrated schematically in Figure 8, for the case of positively reflexed morphing, which requires chordwise contraction at the front slit and expansion at the rear slit. The spar splits the TE in two parts. In the front, displacement due to contraction is translated to a force f_{front} exerted by the pressure side skin on the web. This force generates a clockwise moment on the suction side skin, causing the skin to bend in the direction of the negative z-axis. Conversely, in the rear, displacement due to expansion is translated to a force f_{rear} exerted by the pressure side skin on the suction side skin. This force generates an anti-clockwise moment on the suction side skin, causing the skin to bend in the direction of the positive z-axis. Combined, these effects cause the change in curvature sign, associated with reflexed airfoils. To achieve this it is crucial to tune the spar stiffness appropriately. Excessive stiffness increases the required actuation forces. Conversely, excessive flexibility deforms the web, reducing the magnitude of the exerted moments. Hence, $1.5mm$ thickness steel sheet was found to strike that balance. The spar web also features two slender gaps, allowing access to push rods and reducing its torsional stiffness, thereby promoting twist morphing. However, a web is included between the gaps connecting the two skins in the middle of the flap, thereby mitigating skin deflection due to suction resulting from lower pressure in the exterior.

Numerical analysis toolchain

In Section 3 a conceptual design is proposed with the aim of achieving the desired morphing functionality. A set of components and features are therefore selected, each contributing to the above objective. In Section 5 numerical analysis results are used to assess the concept's functionality. This section presents the numerical analysis toolchain developed for that purpose. The analysis revolves around the FEM of the morphing flap structure, modelled in MSC Nastran. The FEM is shown in Figure 9, including annotations indicating the elements corresponding to the key components. Visual access to the flap interior mesh is obtained by removing some suction skin elements.

In total, the FEM is made of 5801 elements. An average element edge length of approximately $10mm$ is maintained across the mesh. Shell elements (CTRIA3, CQUAD4) approximate thin-walled structures like the composite skin, trailing edge spar and 3D-printed frame. Such elements are also used to model the base plate and the TE spar flange. These low thickness components are in contact with the skin and are therefore merged into single shell elements, with layered composite properties (PCOMP). Solid elements (CPENTA6, CHEXA8) are used to model the adaptors used to connect the actuators on either end. These components are significantly stiffer than the surrounding structure, justifying the use of a coarse mesh. Solid elements are also used to model the thick layer of epoxy used to join the two skins along the TE tip.

Beam elements (CBEAM) are used to model the actuators, treating push rods and motors individually. The push rods are modelled realistically using the correct material properties and beam profiles. The structure of the motor housing remains undeformed during operation. It is therefore approximated as rigid. However, beam elements are preferred over rigid-body elements, as the former can be used to simulate displacement along the motor axis by means of thermal strains. Overall, artificial material properties are used in the elements representing the motors. This includes a Young's modulus of $10,000GPa$ and a strain-to-temperature sensitivity value of $1\mu\varepsilon/K$.

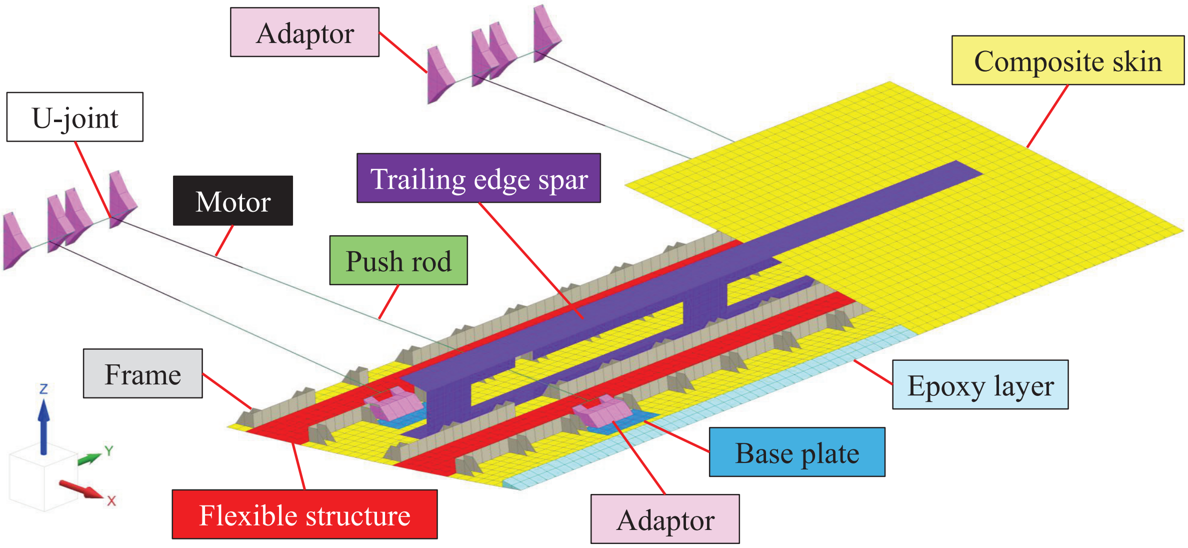

Figure 9. Morphing flap finite element model. Part of the suction side skin mesh is omitted for demonstration purposes, providing visual access to the interior. Annotations indicate the mesh corresponding to key components.

Rigid-body elements are used to connect the actuators to the adaptors. First, RBE2 elements are defined between the arms of the adaptors, with a node at the point of connection. The universal-joints are simulated via RJOINT elements between these nodes and the actuator end nodes. Finally, for the purpose of the analysis, the LE is approximated as quasi-rigid. It is therefore represented via clamped boundary conditions on the skin nodes in the front end of the TE as well as the front adaptor nodes in contact with the front spar.

Overall, the mesh of the FEM is constructed with emphasis on the composite skin, which exhibits significant deformation during morphing. Specifically, for each of the two skins, a 32-by-75 element mesh is used to model the 320mm-by-750mm flap skin. This amounts to a total of 4800 CQUAD4 elements of aspect ratio 1, forming the majority of the elements. The above follows the approach adopted by Mkhoyan et al. (2022) in a past study regarding the development of a camber-twist morphing flap, featuring glass fibre skin of dimensions 200mm-by-300mm. Specifically, they report mesh convergence at a mesh seed size of 10mm. The present study maintains these element dimensions in the context of a larger structure, thereby further refining the mesh.

An alternative modelling approach is taken for the flexible skin structure. The approach aims to capture the structure's stiffness properties whilst limiting element count and avoiding rod-bushing contact modelling, thereby reducing computational cost and improving computational stability. Hence, the structure is approximated as a shell with anisotropic membrane and bending stiffness. The above resembles a laminate, hence its constitutive equation is given from classical laminated plate theory (Kassapoglou, 2013). The stiffness matrix is made of two symmetric matrices: the membrane stiffness $\bar{\bar{A}}$ and the bending stiffness $\bar{\bar{D}}$. The former relates in-plane loads $\vec{n} = [n_x, n_y, n_{xy}]^T$ to membrane strains $\vec{\varepsilon} = [\varepsilon_x, \varepsilon_y, \varepsilon_{xy}]^T$. The latter relates bending moments $\vec{m} = [m_x, m_y, m_{xy}]^T$ to curvatures $\vec{\kappa} = [\kappa_x, \kappa_y, \kappa_{xy}]^T$. Minimal coupling effects are observed, hence coupling stiffness $\bar{\bar{B}} = \bar{\bar{0}}$, where $\bar{\bar{0}}$ is the zero matrix. The constitutive equation is given in equation (1).

$$\begin{bmatrix} \vec{n} \\ \vec{m} \end{bmatrix} = \begin{bmatrix} \bar{\bar{A}} & \bar{\bar{0}} \\ \bar{\bar{0}} & \bar{\bar{D}} \end{bmatrix} \begin{bmatrix} \vec{\varepsilon} \\ \vec{\kappa} \end{bmatrix} \tag{1}$$

Calculating $\bar{\bar{A}}$ and $\bar{\bar{D}}$ requires an auxiliary FEM of the flexible structure. The matrices can be calculated by applying unit loads for each component of $\vec{n}$ and $\vec{m}$ and calculating the resulting $\vec{\varepsilon}$ and $\vec{\kappa}$ respectively. The unit loads take the form $\overrightarrow{n_1} = \overrightarrow{m_1} = [1, 0, 0]^T$, $\overrightarrow{n_2} = \overrightarrow{m_2} = [0, 1, 0]^T$ and $\overrightarrow{n_3} = \overrightarrow{m_3} = [0, 0, 1]^T$. The unit in-plane loads result in membrane strains $\overrightarrow{\varepsilon_1}$, $\overrightarrow{\varepsilon_2}$ and $\overrightarrow{\varepsilon_3}$ respectively. Equivalently, the unit bending loads result in curvatures $\overrightarrow{\kappa_1}, \overrightarrow{\kappa_2}$ and $\overrightarrow{\kappa_3}$. The above vectors can be assembled in matrix format to calculate $\bar{\bar{A}}$ and $\bar{\bar{D}}$, as shown in equations (2)–(5), where $\bar{\bar{I}}$ is the identity matrix.

$$\begin{bmatrix} \overrightarrow{n_1} & \overrightarrow{n_2} & \overrightarrow{n_3} \end{bmatrix} = \begin{bmatrix} 1 & 0 & 0 \\ 0 & 1 & 0 \\ 0 & 0 & 1 \end{bmatrix} = \bar{\bar{A}} \begin{bmatrix} \overrightarrow{\varepsilon_1} & \overrightarrow{\varepsilon_2} & \overrightarrow{\varepsilon_3} \end{bmatrix} \tag{2}$$

$$\bar{\bar{A}} = \bar{\bar{I}} \begin{bmatrix} \overrightarrow{\varepsilon_1} & \overrightarrow{\varepsilon_2} & \overrightarrow{\varepsilon_3} \end{bmatrix}^{-1} \tag{3}$$

$$\begin{bmatrix} \overrightarrow{m_1} & \overrightarrow{m_2} & \overrightarrow{m_3} \end{bmatrix} = \begin{bmatrix} 1 & 0 & 0 \\ 0 & 1 & 0 \\ 0 & 0 & 1 \end{bmatrix} = \bar{\bar{D}} \begin{bmatrix} \overrightarrow{\kappa_1} & \overrightarrow{\kappa_2} & \overrightarrow{\kappa_3} \end{bmatrix} \tag{4}$$

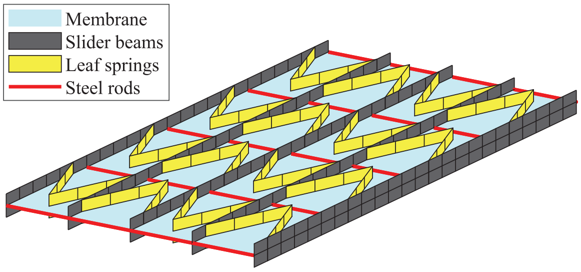

Figure 10. Schematic representation of finite element model of the flexible skin structure. An auxiliary membrane serves as a reference surface for strain and curvature calculation.

$$\bar{\bar{D}} = \bar{\bar{I}}\left[\vec{\kappa_1} \quad \vec{\kappa_2} \quad \vec{\kappa_3}\right]^{-1} \tag{5}$$

A schematic representation of the auxiliary FEM is shown in Figure 10; the depicted pattern is repeated to yield uniform deformation, avoiding boundary effects at the edges. The two stiffness matrices are primarily influenced by the presence of the steel rods. The leaf springs are included to capture chordwise in-plane stiffness. The slider mainly affects spanwise in-plane stiffness and is modelled without the flange for simplicity. The leaf springs and slider beams are modelled with shell elements. The steel rods resist transverse bending whilst allowing axial translation and rotation. To simulate these mechanics, they are treated as Euler-Bernoulli beams. Therefore, their stiffness matrix is calculated analytically and directly added to the corresponding nodes as direct matrix input (DMIG). Finally, an auxiliary membrane is added, covering the mid-plane of the structure normal to the out-of-plane axis. Its material is defined with artificially low stiffness, to ensure it does not affect the structure's overall mechanics. Its purpose is to provide a reference surface to calculate strain and curvature. Static stability is achieved via clamped boundary conditions at a node in the centre of the membrane mesh. A set of unit $\vec{n}$ and $\vec{m}$ is applied and the stiffness matrices $\bar{\bar{A}}$ and $\bar{\bar{D}}$ are extracted. Ultimately, these properties are assigned to the shell elements representing the flexible structure in the FEM of the flap.

Based on the developed FEM, a nonlinear static aeroelastic analysis toolchain is established, iterating between the FEM and XFOIL. The toolchain is presented in the form of a flowchart in Figure 11. To initiate the loop, the four actuator strokes $\vec{q} = [q^A_{front}, q^A_{rear}, q^B_{rear}, q^B_{front}]^T$ are imposed and a nonlinear static analysis is performed without aerodynamic loads. Actuator strokes are simulated via thermal expansion or contraction, by imposing the corresponding temperature difference (TEMP2) to the actuator nodes. The nonlinear static solver SOL106 is chosen, to account for large displacements and rotations. The skin displacement field is extracted and processed to calculate the morphed skin position field $\vec{x}$. Henceforth, the iterative analysis is initiated. Having prescribed α and Re, $\vec{x}$ is added to the constant LE shape and the flap is segmented into a set of airfoils along the span. XFOIL performs 2D steady aerodynamic analysis on each airfoil, calculating the 2D pressure distribution $\overrightarrow{C_p}$ and polars C_l, C_d and C_{mac}. The extracted $\overrightarrow{C_p}$ are combined to yield the 3D pressure distribution, as shown in Figure 12. The set of airfoils used to run XFOIL are also plotted along the span of the morphed trailing edge shape. The static analysis is repeated with the addition of aerodynamic loads in the form of pressure loads (PLOAD2) on the skin. The analysis yields an updated $\vec{x}$, as well as the corresponding actuator forces $\vec{f} = [f^A_{front}, f^A_{rear}, f^B_{rear}, f^B_{front}]^T$, measured as reaction forces on the constrained front adaptor nodes. The two latest $\vec{x}$ fields are used to determine convergence by calculating the root mean square difference δ_{rms} between the two skin displacement fields. The updated $\vec{x}$ is fed back into XFOIL until δ_{rms} falls below a given tolerance value δ_{tol} and convergence is reached.

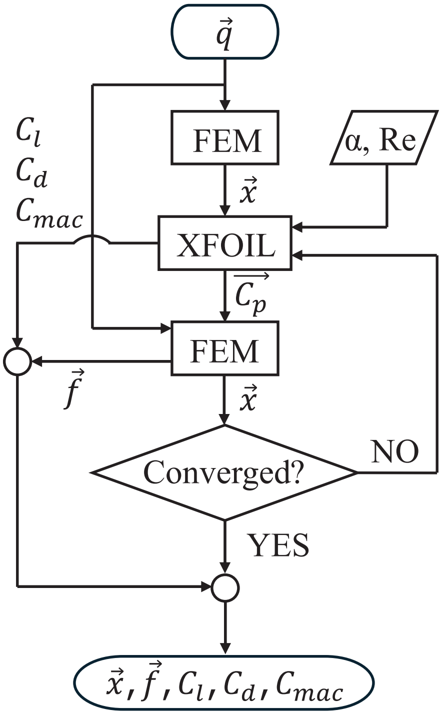

Figure 11. Numerical analysis flowchart. The tool iterates between nonlinear static finite element analysis and 2D steady viscous aerodynamic analysis.

Two distinctions are made regarding the aerodynamic analysis. First, in the presence of asymmetric morphing, the analysis fails to capture the influence of crossflow. Crossflow affects primarily boundary layer

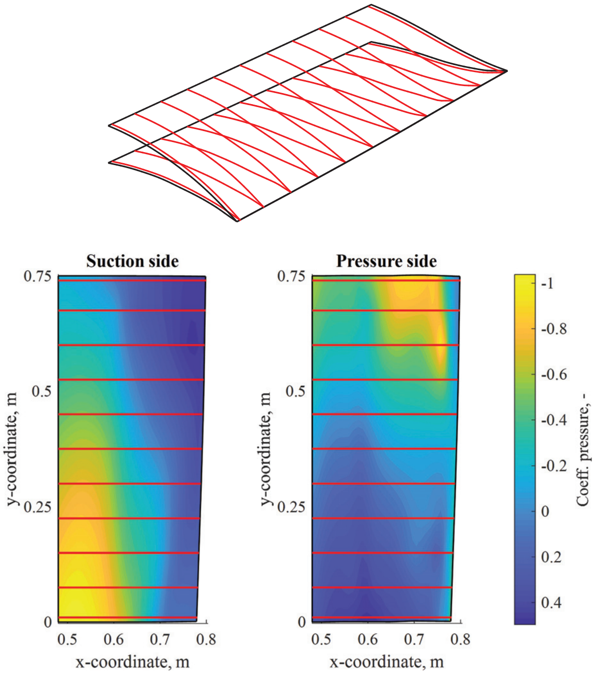

Figure 12. Numerical analysis results. A morphing trailing edge is presented in terms of shapes projected on planes parallel to the x-z plane. Contour plots projected on the respective flap skins represent the interpolated pressure distribution. Red lines indicate the spanwise position of the projected airfoils.

flow, hence C_d results are omitted. However, given the attainable degree of twist morphing, the influence of crossflow on $\overrightarrow{C_p}$ is deemed limited. Crucially, the primary purpose of reconstructing the pressure distribution is to assess the flap's ability to morph in the presence of aerodynamic loads and to study the resulting morphed shape. Given the above, despite some error in individual $\overrightarrow{C_p}$ calculation, the overall effect of aerodynamic loading on the morphing flap is captured with sufficient accuracy. Second, the pressure differential used in the PLOAD2 entries is calculated using an estimate of the internal static pressure p_0. Pressure leaks are anticipated along the flap through the pressure side skin slits or the spanwise ends of the flap, making the prediction of p_0 uncertain. Hence, a choice is made to equate p_0 to the pressure corresponding to the highest calculated C_p value. This overestimates suction, leading to exaggerated outwards skin bulging. These deflections compromise the aerodynamic performance of the morphed airfoil shapes and must be accounted for in the design phase. Ultimately, this conservative approach is effective in tailoring the skin thickness, such that skin bulging is mitigated.

Morphing flap functionality assessment

The performance of the proposed morphing flap concept is assessed numerically. All XFOIL runs were performed with the maximum Re and q attainable by the envisioned wind tunnel, as defined in Section 2.

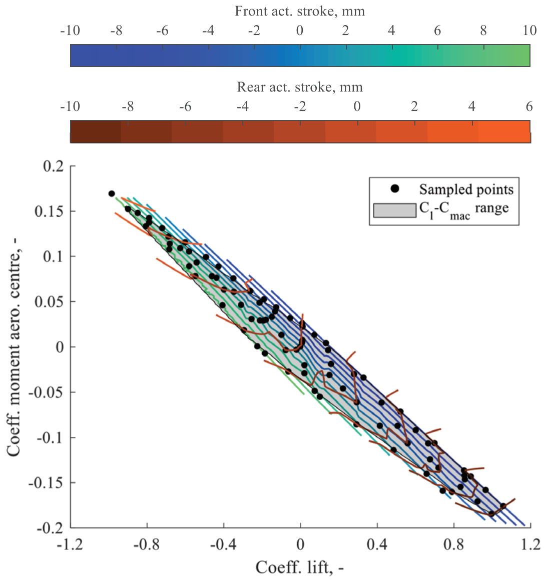

Figure 13. Camber morphing range defined as a cluster in the C_l-C_{mac} plane for $\alpha = 0°$. Sampled points and isolines indicate the mapping between actuator strokes and aerodynamic polars.

The range of the camber morphing functionality is shown in Figure 13, in terms of attainable C_l-C_{mac} combinations for $\alpha = 0°$; no twist morphing is present in this dataset. The sampled points form an ellipse-like polygonal cluster, validating the concept's ability to decouple C_{mac} from C_l. The shape of the cluster resembles the theoretical potential presented in Section 2, where the range of attainable C_{mac} for a given value of C_l gradually decreases as C_l increases. The cluster boundaries are determined by either actuator stroke or force limits; component interference and material failure would have been critical in the presence of larger stroke and force range. The sample points outside the cluster boundaries exceed the actuator force limits and are therefore unattainable.

The isolines indicate the actuator stroke settings required to achieve a given C_l-C_{mac} combination. The values on the colorbars correspond to the depicted stroke levels. It is noted that the rear actuator stroke q_{rear} is limited to a maximum of under $6mm$ due to excessive actuator force requirements. The isoline spacing is kept constant at $2mm$ stroke, thereby revealing the polars' sensitivity to each actuator. For given front actuator stroke q_{front}, a step increase in q_{rear} causes a large change in the general direction of the cluster's major axis, resembling 1-DoF morphing. Graphically, this corresponds to selecting one of the blue-green isolines and spanning its length in the direction of negative C_l. Conversely, for given q_{rear}, a step increase in q_{front} causes a small change in the general direction of the cluster's minor axis. Graphically, this corresponds to

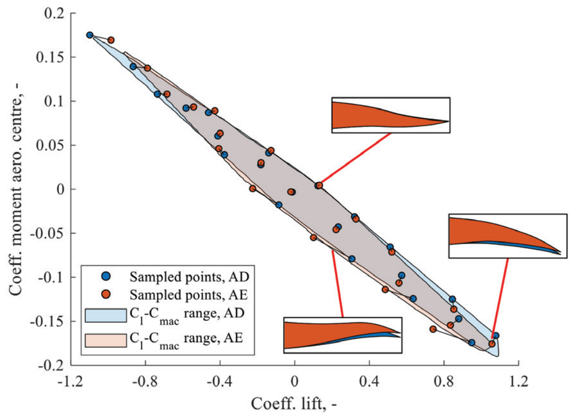

Figure 14. Influence of aeroelastic deflections on the morphing functionality for $\alpha = 0^\circ$. Clusters demonstrate the change in camber morphing range as a result of aeroelastic deflections. Sampled points indicate the change in C_l and C_{mac} as a result of deflections. Highlighted trailing edge shapes depict the change in geometry experienced by different types of morphing shapes.

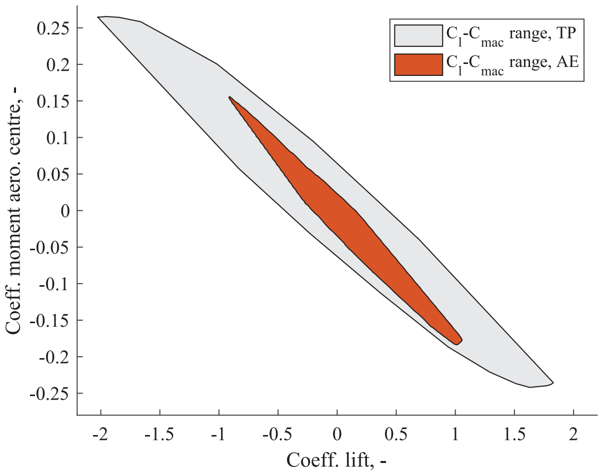

Figure 15. Attainable camber morphing range relative to the theoretical limit at $\alpha = 0^\circ$. The difference in range is expressed in terms of the two clusters plotted in the C_l-C_{mac} plane.

choosing one of the brown-orange isolines and spanning its length in the direction of negative C_{mac}. From minimum to maximum q_{front}, the airfoil evolves from a positively to a negatively reflexed shape.

As discussed in Section 3, the choice of an open-loop linkage in conjunction with a flexible skin introduces aeroelastic deflections. Their effect on the camber morphing functionality is presented in Figure 14 for $\alpha = 0^\circ$. Two clusters are presented, one before and one after aeroelastic effects. The former is calculated by the first XFOIL run, using shapes obtained before aerodynamic loads were introduced to the FEM; this dataset is labelled "aerodynamic" (AD). The latter is calculated by the final XFOIL run, upon convergence of the loop; this dataset is labelled "aeroelastic" (AE). Solely comparing the size and position of the two clusters, it is concluded that aeroelastic deflections have minimal effect on camber morphing range. The area of the cluster only decreases by 3.74%, as the clusters mostly overlap. However, focussing on how the polars evolve in specific cases, a pattern is observed. Focussing on positive C_l cases, as curvature evolves from positively to negatively reflexed, the change in polars increases, primarily leading to reduced C_l. This is further validated by the change in TE shape, as shown for selected cases. This effect is attributed to the pressure distribution resulting from the curvature. Notably, in the case of negative reflex, aeroelastic deflection induces further morphing, yielding previously unattainable shapes and polars. Finally, an asymmetric effect is observed regarding the maximum lift $C_{l,max}$ and minimum lift $C_{l,min}$. Specifically, $C_{l,max}$ is only limited by 1.95% to $C_{l,max} = 1.06$ whereas $C_{l,min}$ is limited by 15.10% to $C_{l,min} = 0.91$. This difference is attributed to the active constraint at the boundary. For $C_{l,max}$, the boundary is defined by the stroke limit. Hence, in the presence of aerodynamic loads, additional actuator force is available to maintain the stroke settings and the difference in polar values is the result of deflection. Conversely, the $C_{l,min}$ is defined by actuator force limit, making the intended stroke settings infeasible under aerodynamic loads.

In the absence of structural constraints, the ideal morphing flap would reach the theoretical potential presented in Section 2. The developed concept is therefore assessed relative to that potential; this dataset is labelled "theoretical potential" (TP). In Figure 15 the range of C_l-C_{mac} combinations attainable by the flap is plotted along with the theoretical boundary for $\alpha = 0^\circ$. The aeroelastic cluster is enclosed by the cluster representing the theoretical potential, as expected. In terms of cluster area, the range is reduced by 77.47%. The attainable $C_{l,max}$ is reduced by 42.1%, from 1.83 to 1.06. Similarly, $C_{l,min}$ is reduced by 55.2%, from -2.02 to -0.91. The aeroelastic cluster is skewed towards negatively reflexed shapes in the positive C_l range and positively reflexed shapes in the negative C_l range.

Regarding aerodynamic efficiency, the maximum C_l/C_d attainable by the morphing flap is plotted over a range of α in Figure 16, relative to the theoretical potential presented in Section 2. The trends observed in Figure 4 are maintained. In the lower α range, a sharp increase in C_l/C_d is observed below $\alpha = -3^\circ$, followed by a range of α where the attainable C_l/C_d is up to 14.4% lower at $\alpha = -3^\circ$ but gradually increasing. The

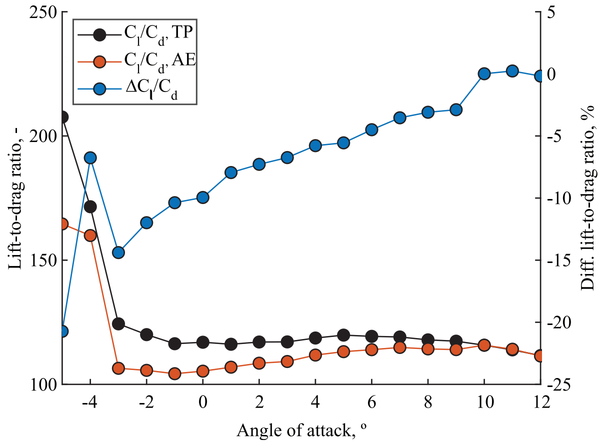

Figure 16. Attainable C_l/C_d relative to the theoretical limit over a range of α. The corresponding percentage difference in C_l/C_d is also plotted.

$\Delta C_l/C_d$ is eliminated in the upper α range, indicating that the corresponding optimal shapes are attainable by the flap. Overall, the flap maintains a C_l/C_d of over 104.3 over the full range of α.

Finally, the range of the twist morphing functionality is shown in Figure 17, for $\alpha = 0^o$. Quantifying the range of twist morphing is non-trivial. In the context of this study, it is assessed in terms of the range of attainable shapes on one spanwise end of the flap, labelled "B," for given actuator settings on the other end, labelled "A." The free end of the flap is characterised by the shape projected on the x-z plane at the 90%-span position; these projections are shown in Figure 12. As discussed in Section 4, the $\overrightarrow{C_p}$ calculated in the presence of asymmetric morphing are compromised as a result of crossflow. Nevertheless, the use of the C_l and C_{mac} corresponding to the projected shape is an effective tool to demonstrate the shapes attainable by the free end of the flap. The polars corresponding to the projected shape are calculated and presented in Figure 17, their boundaries defined by the actuator stroke and force limits. The aeroelastic camber morphing range is plotted for comparison. The range is determined by the actuator settings on end A, hence clusters are presented for three cases, along with a point indicating the C_l-C_{mac} combination corresponding to symmetric actuation, shown as a single marker. The fixed end stroke settings considered are $\{q^A_{front}, q^A_{rear}\} = \{0, 0\}mm$, $\{-10, -10\}mm$ and $\{-10, -1\}mm$, corresponding to Case 1: baseline shape, Case 2: high C_l shape and Case 3: positively reflexed shape. The Case 1 cluster covers 75.2% of the aeroelastic range, including all types of shapes. The Case 2 cluster covers 26.8% of that range, limited to high C_l shapes with emphasis on positively reflexed shapes. The Case 3 cluster covers 38.9% of the range, alternating between positively reflexed shapes in the negative C_l range and negatively reflexed shapes in the positive C_l range. Interestingly, the settings of the fixed end are not attainable under symmetric actuation, as they require excessive actuation force. Hence the marker is plotted outside the aeroelastic cluster. However, they become attainable when combined with the appropriate settings on the other end. This is attributed to a reduction in strain energy despite the asymmetric skin shape. Overall, the range of shapes attainable by one end of the flap is coupled to the fixed actuator strokes on the other end.

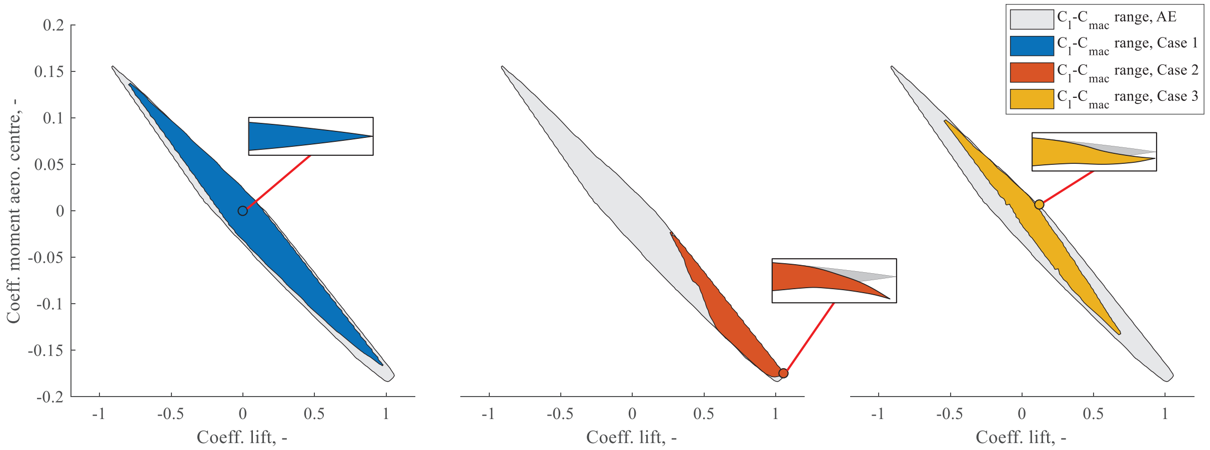

Figure 17. Twist morphing range expressed in terms of the range of shapes attainable by the free end of the flap, for given actuator strokes on the fixed end, for $\alpha = 0°$. Clusters are presented for three cases of fixed end strokes, corresponding to the highlighted shapes.

Conclusion

The central motivation of this paper was to present a novel camber-twist morphing flap concept. Using the TRIC concept as inspiration, a flap design was obtained capable of morphing into reflexed airfoil shapes, whilst maintaining the twist morphing functionality.

The reflexed airfoil morphing functionality was first explored in terms of an arbitrary morphing flap's ability to obtain a wide range of C_l-C_{mac} combinations and maximise C_l/C_d over a range of α. The TP dataset was calculated using XFOIL, by globally sampling TE geometries, subject to a set of boundary conditions. For each α value, the samples form clusters in the C_l-C_{mac} plane. The ellipse-like cluster shape represents the ability to decouple C_{mac} from C_l.

The following notable design features combine to achieve the desired morphing functionality. Two spanwise slits combine to yield conformal as well as reflexed airfoil morphing. The discontinuous skin was joined by a flexible structure capable of chordwise translation by means of chordwise leaf springs and steel rods. A TE spar was introduced between the two slits, capable of transmitting the moments necessary to morph into reflexed shapes. A total of four linear electric motors were included, necessary to combine the reflexed airfoil with the twist morphing functionality. Universal joints were used to connect the actuators to the structure resulting in an open-loop linkage which does not prevent aeroelastic deflections. The flap design was translated to a FEM and a nonlinear static aeroelastic analysis toolchain was established as a loop between FEM and XFOIL.

The attainable range of C_l-C_{mac} was calculated, as determined by actuator stroke and force limits. The boundaries form an ellipse-like cluster validating the concept's ability to decouple C_{mac} from C_l. Isolines representing stroke levels revealed the polars' sensitivity to the respective actuators. Comparing results before and after aeroelastic deflections, the magnitude of deflection, and hence change in polars, was found to depend on the pressure distribution, as dictated by the airfoil shape. Negatively reflexed shapes deflected the most, whereas positively reflexed shapes were marginally affected. The AE cluster area was reduced by only 3.74% relative to the AD cluster, validating the morphing functionality in the presence of aeroelastic deflections.

Compared to its theoretical potential, the AE cluster was reduced by 77.47%. At $\alpha = -5°$, $\Delta C_l/C_d = -20\%$ indicating that the flap cannot morph into the desired shape. However, as α increases, this gap is gradually reduced and fully eliminated from $\alpha = 10°$ onwards, indicating the flap's ability to morph into these optimal shapes.

When varying stroke settings on the free end, the range of twist morphing functionality was found to depend on the actuator strokes on the fixed end of the flap. The Case 1 cluster covers 75.2% of the camber morphing range, including all types of shapes. The Case 2 cluster covers 26.8% of that range, limited to high C_l shapes with emphasis on positively reflexed shapes. The Case 3 cluster covers 38.9% of the range, alternating between positively reflexed shapes in the negative C_l range and negatively reflexed shapes in the positive C_l range.

Acknowledgements

The authors acknowledge the partnering organisations from the RICHTING project: Dutch-German Wind Tunnels (DNW), Royal Netherlands Aerospace Laboratory (NLR), Qlayers, Netherlands Organisation for Applied Scientific Research (TNO).

ORCID iDs

Panagiotis Georgopoulos https://orcid.org/0009-0006-6333-0914
Jurij Sodja https://orcid.org/0000-0001-8347-1438
Roeland De Breuker https://orcid.org/0000-0002-7882-2173

Funding

The authors disclosed receipt of the following financial support for the research, authorship, and/or publication of this article: The authors acknowledge the financial support of the Dutch government through the Netherlands Enterprise Agency (RVO) under the TSH Vliegtuigmaakindustrie programme, project number TSH21009. The RICHTING project (Radicale weerstands en gewICHTsreductie door morphING en microstructuren) started on January 1st 2022 and was concluded successfully on June 30th 2025.

Declaration of conflicting interests

The authors declared no potential conflicts of interest with respect to the research, authorship, and/or publication of this article.

Data availability statement

Data sharing not applicable to this article as no datasets were generated or analysed during the current study.

References

Adeel-Ur-Rehman A, Theron JN, Kassem H, et al. (2024) Improved performance of k $-\omega$ SST turbulence model in predicting airfoil characteristics for a wide range of airfoil thicknesses. *Journal of Physics Conference Series* 2767(2): 022064. Available at: https://doi.org/10.1088/1742-6596/2767/2/022064

Anderson JD (2016) *Introduction to Flight, Chapter 6*. McGraw-Hill Education. pp. 441–593.

Barbarino S, Bilgen O, Ajaj RM, et al. (2011) A review of morphing aircraft. *Journal of Intelligent Material Systems and Structures* 22(9): 823–877. Available at: https://doi.org/10.1177/1045389x11414084

Bubert EA, Woods BKS, Lee K, et al. (2010) Design and fabrication of a passive 1D morphing aircraft skin. *Journal of*

Intelligent Material Systems and Structures 21(17): 1699–1717. Available at: https://doi.org/10.1177/1045389X10378777

Cavalieri V, Gaspari AD and Ricci S (2024) Aero-structural design optimization of a morphing aileron considering actuation aspects. In: *Proceedings of the AIAA SCITECH 2024 forum*, Orlando, FL, USA. DOI:10.2514/6.2024-2113.

De Breuker R, Mkhoyan T, Nazeer N, et al. (2022) Overview of the Smart-X wing technology integrator. *Actuators* 11(10): 302. Available at: https://doi.org/10.3390/act11100302

De Gaspari A, Ricci S, Antunes A, et al. (2014) Application of active camber morphing concept to a regional aircraft. In: *Proceedings of the 22nd AIAA/ASME/AHS adaptive structures conference 2014*, National Harbor, MD, USA. DOI:10.2514/6.2014-1259.

Derksen RW and Rogalsky T (2010) Bezier-PARSEC: An optimized aerofoil parameterization for design. *Advances in Engineering Software* 41(7-8): 923–930. Available at: https://doi.org/10.1016/j.advengsoft.2010.05.002

Drela M (1989) XFOIL: An analysis and design system for low Reynolds number airfoils. In: Muelle TJ (ed.) *Low Reynolds Number Aerodynamics*, vol. 54. Springer. pp. 1–12.

German-Dutch Wind Tunels (n.D) Low-speed tunnel. Available at: https://www.dnw.aero/wind-tunnels/lst/ (accessed 27 September 2025)

Harvey C, Gamble LL, Bolander CR, et al. (2022) A review of avian-inspired morphing for UAV flight control. *Progress in Aerospace Sciences* 132: 100825. Available at: https://doi.org/10.1016/j.paerosci.2022.100825

Jenett B, Calisch S, Cellucci D, et al. (2017) Digital morphing wing: Active wing shaping concept using composite lattice-based cellular structures. *Soft Robotics* 4(1): 33–48. Available at: https://doi.org/10.1089/soro.2016.0032

Jensen LL, Bonnefoy PA, Hileman JI, et al. (2023) The carbon dioxide challenge facing U.S. Aviation and paths to achieve net zero emissions by 2050. *Progress in Aerospace Sciences* 141: 100921. Available at: https://doi.org/10.1016/j.paerosci.2023.100921

Kassapoglou C (2013) *Design and Analysis of Composite Structures, Chapter 3*. John Wiley & Sons, Ltd. pp. 33–53.

Keidel D, Fasel U and Ermanni P (2021) Concept investigation of a lightweight composite lattice morphing wing. *AIAA Journal* 59(6): 2242–2250. Available at: https://doi.org/10.2514/1.J059579

Kota S, Flick P and Collier FS (2016) Flight testing of flexfloil adaptive compliant trailing edge. In: *Proceedings of the 54th AIAA aerospace sciences meeting 2016*, San Diego, CA, USA. DOI:10.2514/6.2016-0036.

McGowan AMR, Washburn AE, Horta LG, et al. (2002) Recent results from NASA's morphing project. In: *Proceedings of the SPIE 9th annual international symposium on smart structures and materials: Industrial and commercial applications of smart structures technologies*, San Diego, CA, USA, vol. 4698, pp. 97–111. DOI:10.1117/12.475056.

Mkhoyan T, Ruland O, De Breuker R, et al. (2023) On-line black-box aerodynamic performance optimization for a morphing wing with distributed sensing and control. *IEEE Transactions on Control Systems Technology* 31(3): 1063–1077. Available at: https://doi.org/10.1109/TCST.2022.3210164

Mkhoyan T, Thakrar NR, De Breuker R, et al. (2022) Morphing wing design using integrated and distributed trailing edge morphing. *Smart Materials and Structures* 31(12): 125025. Available at: https://doi.org/10.1088/1361-665X/aca18b

Molinari G, Arrieta AF, Guillaume M, et al. (2016) Aero-structural performance of distributed compliance morphing wings: Wind tunnel and flight testing. *AIAA Journal* 54(12): 3859–3871. Available at: https://doi.org/10.2514/1.J055073

Moulton B and Hunsaker DF (2021) 3D-printed wings with morphing trailing-edge technology. In: *Proceedings of the AIAA SCITECH 2021 forum*, Virtual event. DOI:10.2514/6.2021-0351.

MSC Software Corporation (2019) MSC Nastran 2019 FP1 Quick reference guide. Available at: https://simcompanion.hexagon.com/customers/s/article/msc-nastran-2019-fp1-qu ick-reference-guide-doc12164 (accessed 28 September 2025)

MSW Motion Control GmbH (n.D) Elektrozylinder DSZY1-POT (MIT potentiometer). Available at: https://www.msw-motion.de/produkt/dszy1-pot/ (accessed 28 September, 2025)

Nguyen N, Lebofsky S, Ting E, et al. (2015) Development of variable camber continuous trailing edge flap for performance adaptive aeroelastic wing. In: *Proceedings of the SAE aerotech congress & exhibition*, Seattle, WA, USA. DOI:10.4271/2015-01-2565.

Pankonien AM, Faria CT and Inman DJ (2015) Synergistic smart morphing aileron: Experimental quasi-static performance characterization. *Journal of Intelligent Material Systems and Structures* 26(10): 1179–1190. Available at: https://doi.org/10.1177/1045389x14538530

Pecora R (2021) Morphing wing flaps for large civil aircraft: Evolution of a smart technology across the clean sky program. *Chinese Journal of Aeronautics* 34(7): 13–28. Available at: https://doi.org/10.1016/j.cja.2020.08.004

Pendleton EW, Bessette D, Field PB, et al. (2000) Active aeroelastic wing flight research program: Technical program and model analytical development. *Journal of Aircraft* 37(4): 554–561. Available at: https://doi.org/10.2514/2.2654

Perry B, Cole SR and Miller GD (1995) Summary of an active flexible wing program. *Journal of Aircraft* 32(1): 10–15. Available at: https://doi.org/10.2514/3.46677

Powers S, Webb L, Friend E, et al. (1992) Flight test results from a supercritical mission adaptive wing with smooth variable camber. In: *Proceedings of the 6th AIAA biennial flight test conference 1992*, Hilton Head Island, SC, USA. DOI:10.2514/6.1992-4101.

Sanders B, Crowe R and Garcia E (2004) Defense advanced research projects agency – Smart materials and structures demonstration program overview. *Journal of Intelligent Material Systems and Structures* 15(4): 227–233. Available at: https://doi.org/10.1177/1045389x04042793

Schweiger J, Suleman A, Kuzmina S, et al. (2002) MDO concepts for a European research project on active aeroelastic aircraft. In: *Proceedings of the 9th AIAA/ISSMO Symposium on multidisciplinary analysis and optimization 2002*, Atlanta, GA, USA. DOI:10.2514/6.2002-5403.

Vasista S, Tong L and Wong KC (2012) Realization of morphing wings: A multidisciplinary challenge. *Journal of Aircraft* 49(1): 11–28. Available at: https://doi.org/10.2514/1.C031060

Vos R, Gürdal Z and Abdalla M (2010) Mechanism for warp-controlled twist of a morphing wing. *Journal of Aircraft* 47(2): 450–457. Available at: https://doi.org/10.2514/1.39328

Wang X, Mkhoyan T, Mkhoyan I, et al. (2021) Seamless active morphing wing simultaneous gust and maneuver load alleviation. *Journal of Guidance Control and Dynamics* 44(9): 1649–1662. Available at: https://doi.org/10.2514/1.G005870

Weisshaar TA (2013) Morphing aircraft systems: Historical perspectives and future challenges. *Journal of Aircraft* 50(2): 337–353. Available at: https://doi.org/10.2514/1.C031456

Werter N, Sodja J, Spirlet G, et al. (2016) Design and experiments of a warp induced camber and twist morphing leading and trailing edge device. In: *Proceedings of the 24th AIAA/AHS adaptive structures conference 2016*, San Diego, CA, USA. DOI:10.2514/6.2016-0315.

Wölcken PC and Papadopoulos M (2016) *Proceedings of the final project conference: smart intelligent aircraft structures (SARISTU)*, Springer Cham. ISBN 978-3-319-22413-8.

Woods BK, Bilgen O and Friswell MI (2014) Wind tunnel testing of the fish bone active camber morphing concept. *Journal of Intelligent Material Systems and Structures* 25(7): 772–785. Available at: https://doi.org/10.1177/1045389X14521700

Wu R, Soutis C, Zhong S, et al. (2017) A morphing aerofoil with highly controllable aerodynamic performance. *Aeronautical Journal* 121(1235): 54–72. Available at: https://doi.org/10.1017/aer.2016.113